Radiation induced segregation and precipitation behavior in self-ion irradiated Ferritic/Martensitic HT9 steel

Ce Zheng [a], Maria A. Auger [b], Michael P. Moody [b], Djamel Kaoumi [a], *

[a] Department of Nuclear Engineering, North Carolina State University, Raleigh, 27607, NC, USA
[b] Department of Materials, University of Oxford, Parks Road, OX1 3PH, Oxford, UK

A B S T R A C T

In this study, Ferritic/Martensitic (F/M) HT9 steel was irradiated to 20 displacements per atom (dpa) at 600 nm depth at 420 and 440 °C, and to 1, 10 and 20 dpa at 600 nm depth at 470 °C using 5 MeV Fe++ ions. The characterization was conducted using ChemiSTEM and Atom Probe Tomography (APT), with a focus on radiation induced segregation and precipitation. Ni and/or Si segregation at defect sinks (grain boundaries, dislocation lines, carbide/matrix interfaces) together with Ni, Si, Mn rich G-phase precipitation were observed in self-ion irradiated HT9 except in very low dose case (1 dpa at 470 °C). Some G-phase precipitates were found to nucleate heterogeneously at defect sinks where Ni and/or Si segregated. In contrast to what was previously reported in the literature for neutron irradiated HT9, no Cr-rich α' phase, χ-phases, η phase and voids were found in self-ion irradiated HT9. The difference of observed microstructures is probably due to the difference of irradiation dose rate between ion irradiation and neutron irradiation. In addition, the average size and number density of G-phase precipitates were found to be sensitive to both irradiation temperature and dose. With the same irradiation dose, the average size of G-phase increased whereas the number density decreased with increasing irradiation temperature. Within the same irradiation temperature, the average size increased with increasing irradiation dose.

1. Introduction

The harsh and extreme service conditions in Generation IV and fusion reactors imply significant microstructural changes in F/M steels, including defect clustering, dislocation loop formation, void and bubble formation, radiation induced precipitation and segregation [1]. High Cr (9—12 wt.%) Ferritic/Martensitic (F/M) steels are considered as promising candidates for structural materials as well as for fuel cladding in Generation IV reactors and fusion reactors [2] due to their improved irradiation stability, including enhanced swelling resistance (relatively to austenitic steels), and mechanical properties e.g. high-temperature creep resistance [3,4].

Previous studies [5—12] have reported radiation induced precipitation in 12Cr F/M HT9 steel under neutron irradiation. These studies along with the corresponding irradiation facility, temperature and dose are listed in Table 1 in terms of types of radiation induced precipitates. Radiation induced precipitates observed in

neutron irradiated HT9 include Cr-rich α' [5,6,8,9], (M_6X) η phase [10,12], χ-phases [8] and G-phase [5—7,9,11]. It has been reported that these radiation induced precipitates in F/M alloys may cause severe hardening and embrittlement [13—15], which render the F/M alloys unsuitable for advanced reactor applications. Moreover, the high-temperature strength of F/M steels relies on the stability of secondary phases under neutron irradiation at operating temperatures [16]. Radiation induced segregation is an important factor for the formation and stability of new phases in F/M steels.

While radiation induced precipitation and segregation in neutron irradiated HT9 have been widely reported in the literature, similar investigations in ion irradiated HT9 have only been reported in a few studies [17—19]. Kai et al. [17] observed the formation of Cr-rich α' precipitates in HT9 under 14 MeV Ni ion irradiation to 200 displacements per atom (dpa) at 30—600 °C. Getto et al. [18,19] reported the evolution of microstructure features in self-ion irradiated HT9 at very high damage levels (up to 650 dpa at 460 °C). G-phase and M_2X precipitates as well as voids were observed in self-ion irradiated HT9.

In the present work, self-ion irradiated HT9 to 20 dpa (at 600 nm depth) at 420 and 440 °C, and to 1, 10 and 20 dpa (at 600 nm depth)

* Corresponding author.
  E-mail address: djamelkaoumi@gmail.com (D. Kaoumi).

Table 1
Radiation-induced precipitation in HT9 under neutron or ion irradiation reported in the literature. FFTF: Fast Flux Test Facility; Phénix: French fast neutron reactor; HFIR: High Flux Isotope Reactor.

Precipitate	Irradiation Facility	Temperature (°C)	Dose (dpa)	Reference
α'	FFTF	380−504	155	[5–7]
		420	35	[8]
		420	200	[9]
	Phénix	400−530	30−116	[10]
	14 MeV Ni	300−600	200	[17]
$(M_6X)\eta$	FFTF	407	47	[12]
	Phénix	419	79	[10]
Chi (χ)	FFTF	420	35	[8]
G	FFTF	420	200	[9]
		380−504	155	[5,6]
		384	28	[7]
	HFIR	500	38	[11]
	5 MeV Fe	460	up to 650	[18,19]

at 470 °C were examined using ChemiSTEM and Atom Probe Tomography (APT), which are two techniques well adapted to the detection and characterization of nano-scaled radiation-induced precipitation and segregation. Such systematic study is necessary to investigate the possibility to use ion irradiation to emulate the irradiated microstructures induced by neutron irradiation. Indeed, in contrast with neutron irradiation, ion irradiation can be done under well-controlled conditions (temperature, dose, dose rate), it is less time and cost consuming, as well as no material activation is induced.

2. Experimental

2.1. Materials and irradiation conditions

The chemical composition of HT9 is given in Table 2. The 12Cr F/M alloy HT9 (heat 84425) used in this study had undergone a heat treatment consisting of 1038 °C/5 min and air cooling followed by 760 °C/30 min and air cooling, which resulted in a tempered martensitic structure. Bulk HT9 specimens of dimensions of 20 mm × 1.5 mm x 1.5 mm were irradiated at the Michigan Ion Beam Laboratory (MIBL), University of Michigan using 5 MeV Fe^{++} ions. The specimens were irradiated to 20 dpa at 600 nm depth at 420 and 440 °C, and to 1, 10 and 20 dpa at 600 nm depth at 470 °C. The temperatures were selected in relation to irradiation temperatures of the same alloy undertaken in the BOR-60 reactor, and are based on the invariance theory derived by Mansur [20,21,22] and previous work on HT9 [23] which predicted a temperature shift of about 17 °C for the dose rate difference for the two types of irradiations. The dose rate was set approximately to 5×10^{-4} dpa/s. Irradiation temperature was monitored using an infrared camera and four attached Type J thermocouples on bars outside the irradiation region to provide a temperature history during irradiation. The variation of temperature was maintained within ±5 °C. The damage profiles were calculated with SRIM simulation [24]. For SRIM input, displacement energies of metal alloying elements were each set to 40 eV and non-metal alloying elements, such as Carbon, displacement energies were set to be 28 eV [25]. Fig. 1 shows the SRIM output using quick K-P calculation for 5 MeV Fe ion

Table 2
As-received HT9 nominal composition (wt.%).

Fe	Cr	Mo	Ni	Mn	W	V	Si	C	N	P	S
84.89	11.8	1.03	0.51	0.5	0.5	0.33	0.21	0.21	0.01	0.008	0.003
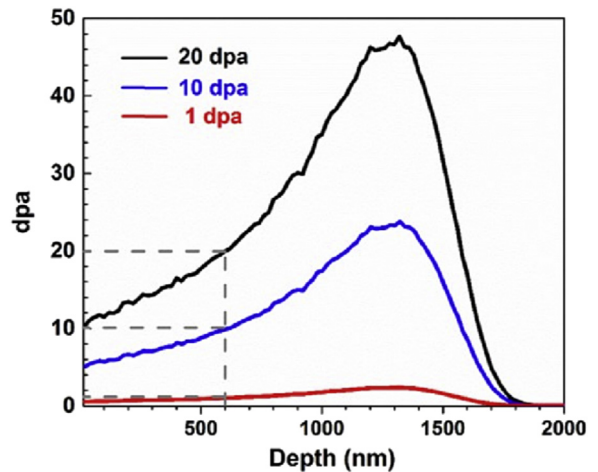
Fig. 1. Damage profiles simulated by SRIM for ion (5 MeV Fe++) irradiated HT9. The shape of damage profiles provide 1, 10 and 20 dpa in the depth of ~600 nm.

irradiation on HT9 alloy. The reported irradiation doses of 1, 10 and 20 dpa correspond to the depth of 600 nm whereas the damage peak is around 1.4 μm depth, according to the SRIM output.

2.2. ChemiSTEM technique

ChemiSTEM characterizations were performed on a FEI Titan 80−300 probe aberration corrected microscope at the Analytical Instrumentation Facility (AIF) at the North Carolina State University. The microscope is equipped with a field emission electron source (X-FEG) and four Bruker SuperX energy dispersive spectrum detectors, which facilitates collection of characteristic X-ray signals at high counts per second and, furthermore, enables mapping of the elemental distribution using ChemiSTEM under Scanning Transmission Electron Microscopy (STEM) mode. For each irradiated HT9 FIB specimen, ChemiSTEM mapping was mainly performed at a depth of ~0.3−1.2 μm from the irradiated surface. This depth range includes the depth (~600 nm) corresponding to relevant doses and avoids the irradiation damage peak and the region of significant implantation.

Although the size and number density of G-phase precipitates were measured on panoramas of Ni maps, the corresponding Si, Mn (and Cr) maps were also used as references in order to only identify G-phase precipitates. In addition, all Ni maps (1024 × 1024 pixel) were taken at the same magnification (×115K) under STEM mode, with a resolution for the Ni maps of 1 pixel ≈ 0.71 nm at this magnification. The size of precipitates is described by the equivalent diameter d_{eq}, which is given as:

$$d_{eq} = \sqrt{a \times b}$$

where a and b are the major axis's length and the minor axis's length of an ellipse, respectively.

TEM specimens were prepared by the lift-out method using a focused ion beam (FIB) system FEI Quanta 3D FEG FIB/SEM at the AIF facility. For each TEM specimen prepared by FIB, the relative thickness ratio (t/λ) was measured using the entire area at a depth up to 1.2 μm by Electron Energy Loss Spectroscopy (EELS). The measured relative thickness ratio (t/λ) was found to be not uniform, and the ratio increases when going from the surface to the deepest depth region. The mean free path of electrons (λ) in HT9 was estimated to be ~90 nm by using the Digital Micrograph script developed by Malis et al. [26]. Input parameters of the mean free

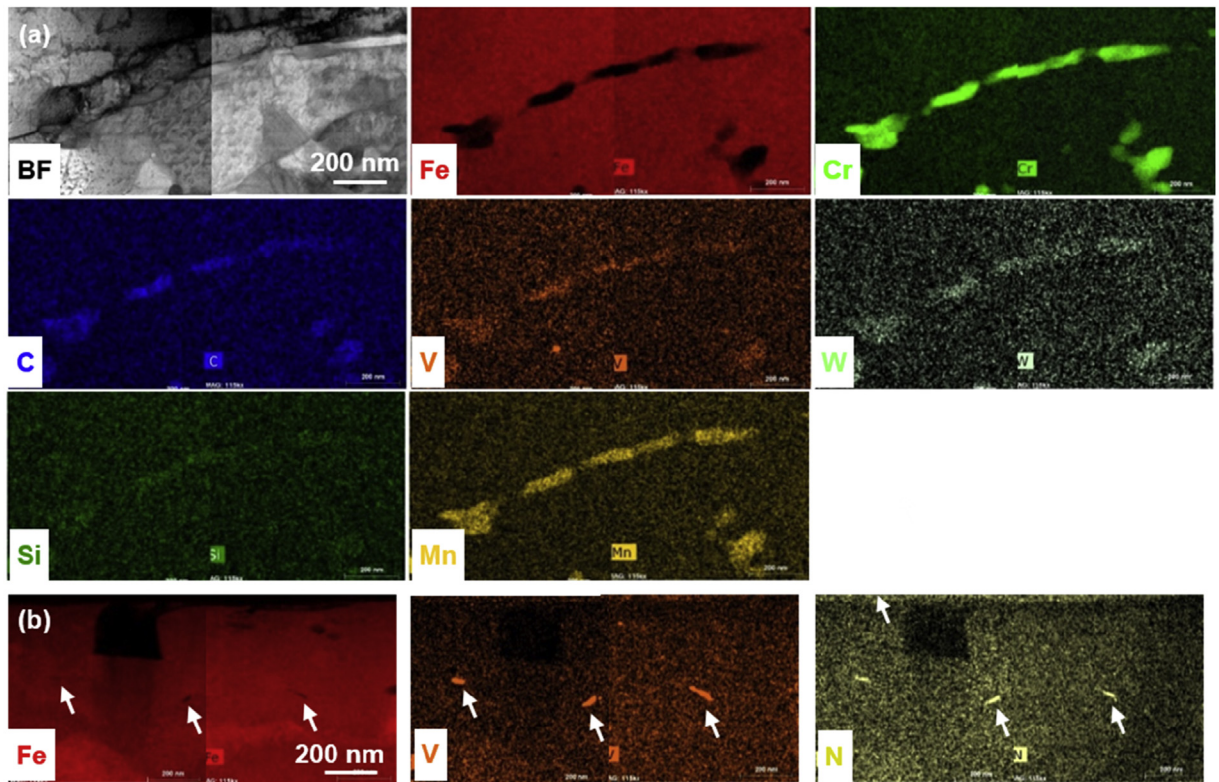**Fig. 2.** ChemiSTEM maps showed the presence of (a) $M_{23}C_6$ carbides and (b) V-rich nitride precipitates in as-received HT9.
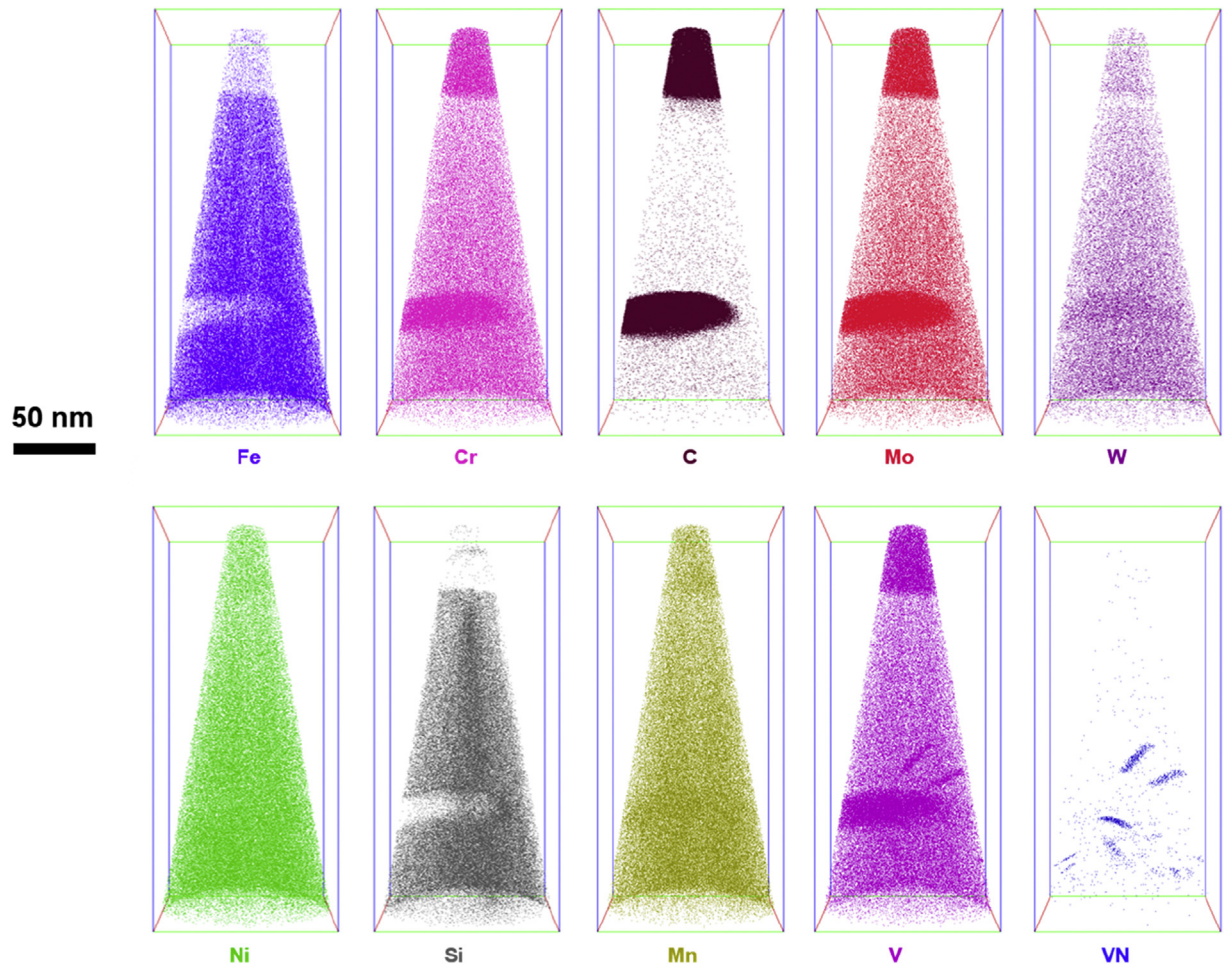

Fig. 3. 3D ion maps confirmed the presence of $M_{23}C_6$ carbides and V-rich nitride precipitates in as-received HT9.

path estimation are compositions (at.%) of HT9, operating tension (200 kV), convergence angle (19.7 mrad) and collection angle (>100 mrad) related to FEI titan microscope. The error of thickness measured by EELS is estimated to be ~10%, as suggested by Malis et al. [26]. In the end, the measured relative thickness of the HT9 FIB-prepared samples was estimated to be between 74 and 150 nm. For the G-phase volume density, the whole area up to 1.2 μm was divided to 12 bins with a bin width of 100 nm. The number of precipitates was then counted in each bin. The local thickness was measured and used to estimate the local volume in each bin.

2.3. Atom probe tomography technique

For APT analysis, the tips were also prepared by the FIB lift-out method using a Zeiss AURIGA 40 FIB/SEM at the University of Oxford and a FEI Helios NanoLab 600i FIB/SEM in the Materials Research Laboratory at the Culham Centre for Fusion Energy. The specimen were extracted from depths of 300 nm–600 nm below surface. The specimen were analyzed using either CAMECA LEAP 3000X HR™ or CAMECA LEAP 5000X HR™ instruments. Either laser or voltage pulsing modes were used. Laser-pulsing mode imposes less stress on the sample and was the first choice so as to improve the yield of successful experiments. Laser-pulsing mode on the LEAP 3000 X HR was used at a repetition rate of 200 kHz, using a laser energy of 0.4 nJ and maintaining the sample temperature at 50–55 K. Three-dimensional (3D) APT data reconstruction and precipitate analysis were carried out using CAMECA IVAS™ software. Multiple APT datasets were successfully obtained for each sample condition, generally between three and five, with the most representative being displayed here. Each dataset contained between 3 and 20 million ions, i.e. the analyzed volumes ranged between 3 and 23×10^{-23} m^3.

3. Results

3.1. As-received HT9

Prior to ion irradiation, as-received HT9 was first examined by the ChemiSTEM and APT techniques, respectively. It is known that HT9 alloy has some typical pre-existing microstructures of F/M steels, including prior austenite grain boundaries (PAGBs), martensitic lath grain boundaries (GBs) and $M_{23}C_6$ carbides forming usually at PAGBs and lath boundaries. In Fig. 2(a), several large size precipitates (>50 nm) were observed along lath boundaries in as-received HT9. These precipitates were identified as $M_{23}C_6$ type carbides containing V, W, Si and Mn, as seen in element maps of Fig. 2(a). In addition, some V-rich nitride precipitates with a smaller size (~20–40 nm) were also observed in as-received HT9, as shown in Fig. 2(b). In addition, the APT analysis confirmed the presence of $M_{23}C_6$ carbides and V-rich nitride precipitates in as-received HT9, as shown in Fig. 3. Beside these two types of features, no other precipitates were observed in as-received condition.
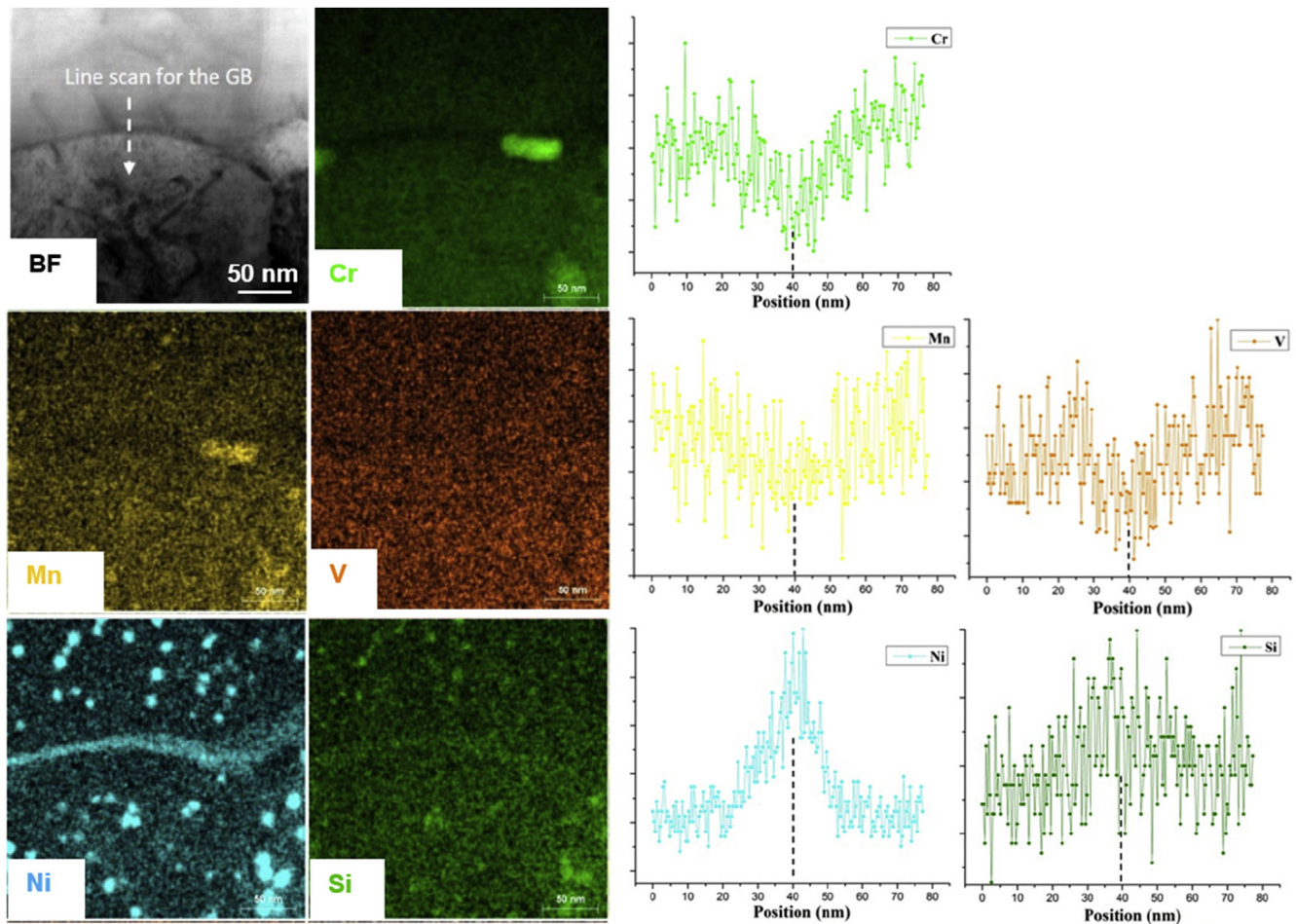
3.2. HT9 irradiated to 20 dpa at 420 °C

As shown in Fig. 4, the enrichment of Ni, Si and Mn was found to associate with the depletion of Fe. The overlapping map of Ni, Si and Mn highlighted the nucleation of Ni, Si, Mn rich precipitates in HT9 irradiated to 20 dpa at 420 °C. These Ni, Si, Mn rich precipitates are known as G-phase. Apart from the presence of G-phase, the segregation of Ni and Si, combined with the depletion of Cr, Mn and V was observed at the same grain boundary, seen in Fig. 5. A large size $M_{23}C6$ carbide was also observed at the grain boundary, as seen in Fig. 5.

The APT analysis also showed Ni and Si segregation at dislocation lines, as shown in Fig. 6(a). The analyzed precipitate (~8 nm) formed at the dislocation line, to which Ni and Si are segregating
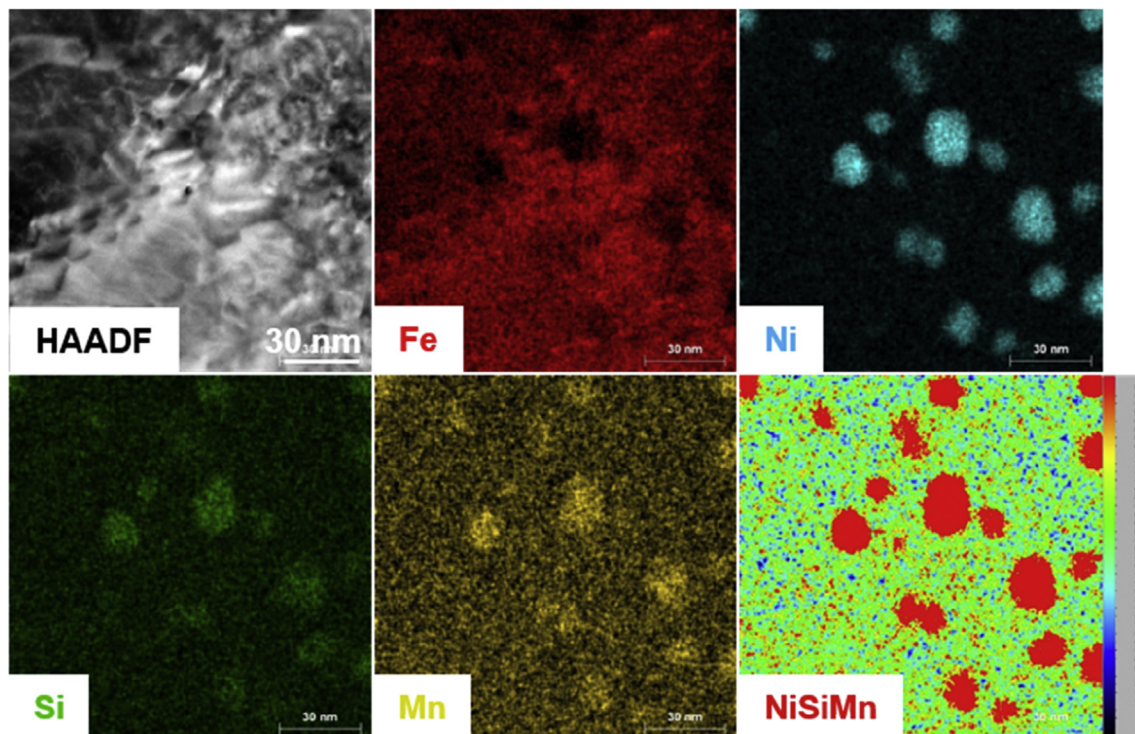
Fig. 4. ChemiSTEM maps (at the irradiation depth ~600–700 nm) showed Ni, Si and Mn enrichment associated with Fe depletion. It indicated the formation of Ni, Si, Mn rich precipitates in HT9 irradiated to 20 dpa at 420 °C.

Fig. 5. In HT9 irradiated to 20 dpa at 420 °C, Ni and Si were found to segregate at the grain boundary where Cr, Mn and V depletion was observed. Ni, Si, Mn rich precipitates were also seen from Ni, Si and Mn maps.

(Fig. 6(b)). A 1D compositional analysis through the analyzed precipitate confirmed formation of G-phase precipitates in HT9 irradiated to 20 dpa at 420 °C, which is in agreement with results obtained by ChemiSTEM. In addition, no Cr-rich α′ phase and voids were observed in this condition.

3.3. HT9 irradiated to 20 dpa at 440 °C

Radiation-induced segregation and precipitation were observed in HT9 irradiated to 20 dpa at 440 °C. Fig. 7 showed the segregation of Ni at the GB and to the carbide/matrix interface together with Ni-rich precipitates. The Ni-rich precipitate (encircled in Fig. 7) was closely investigated by ChemiSTEM at high magnification. Element maps shown in Fig. 8 revealed this Ni-rich precipitate (~7 nm) is actually Ni, Si, Mn rich G-phase precipitate. By comparing bright field micrographs (Fig. 9(a-b)) with corresponding Ni maps (Fig. 9(c-d)), some G-phase precipitates were found to nucleate heterogeneously along lath boundaries and at dislocations in HT9 irradiated to 20 dpa at 440 °C, emphasizing the role of defect sinks as nucleation sites for G-phase precipitation.

Similar results were obtained from the APT observations. Fig. 10(a) displays an APT reconstruction of a HT9 specimen irradiated to 20 dpa at 440 °C. Ni and Si segregation to dislocation lines was also observed. The 1.8 at.% Ni isosurfaces and 1D compositional analysis are displayed in Fig. 10(b) in order to highlight Ni and Si

segregation to dislocation lines in the analyzed volume. According to the geometry of the isosurfaces, it can be presumed that the dislocation lines might be intersecting, as they are located in different planes. Instead of 1.8 at.% isosurfaces, the 8.5 at.% Ni isosurfaces were displayed in Fig. 10(c) in order to highlight Ni-rich precipitates in the analyzed volume. According to the geometry of the isosurfaces, four individual Ni-rich precipitates were identified in the analyzed volume. 1D analysis through one of precipitates (~15 nm) suggests that these are Ni, Si, Mn rich G-phase precipitates. Notably, Cr-rich α′ phase and voids were not observed in this condition.

3.4. HT9 irradiated to 1 dpa at 470 °C

No nucleation of G-phase precipitates was found neither by ChemiSTEM nor by APT in HT9 irradiated to 1 dpa at 470 °C. However, Ni enrichment was found to correlate with Cr and Mn depletion at the same grain boundary by ChemiSTEM, as shown in Fig. 11. Ni and Si segregation to dislocation lines was also observed in the APT analysis, as shown in Fig. 12(a). The application of a 2.0 at. % Ni isosurface is presented in Fig. 12(b) in order to highlight the Ni segregation to the dislocation lines present in the analyzed volume. The 1D compositional analysis in Fig. 12(c) confirms segregation of Ni and Si to the dislocation lines. Again, no Cr-rich α′ phase and voids were observed in this condition.
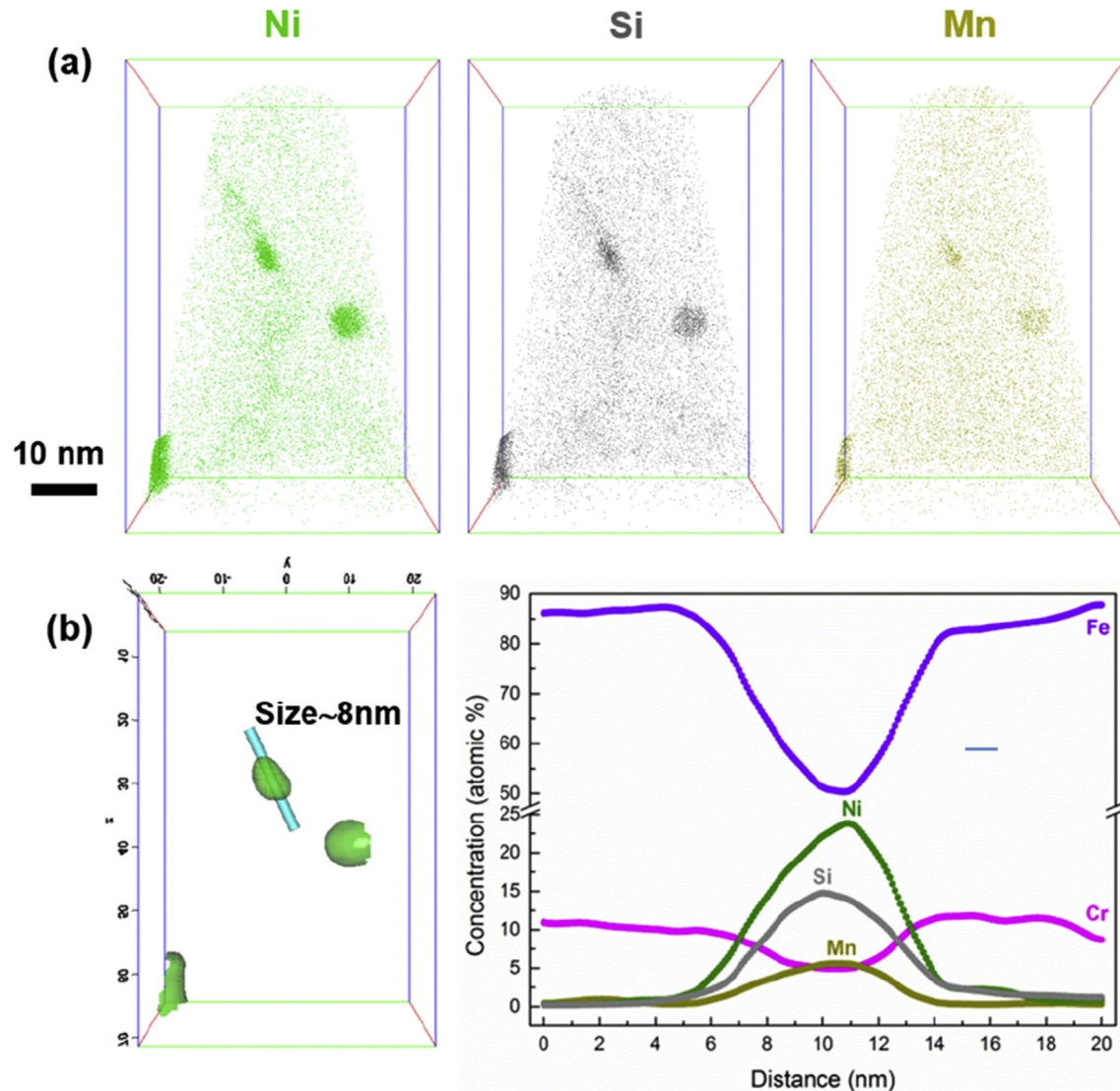
Fig. 6. (a). 3D ion maps from HT9 irradiated to 20 dpa at 420 °C. Ni and Si segregation to a dislocation line together with Ni, Si, Mn rich precipitates were observed here. (b). 1D analysis cylinder through one of Ni, Si, Mn rich precipitates in HT9 irradiated to 20 dpa at 420 °C.

3.5. HT9 irradiated to 10 dpa at 470 °C

Fig. 13 (top) shows Ni segregation at the GB and to the carbide/matrix interface. While a Ni-rich precipitate was observed in Ni map, it is hard to identify directly if this precipitate was also enriched in Si and Mn through the maps of Si and Mn, as shown in Fig. 13 (top). Therefore, the comparison of EDS spectra between the precipitate and matrix was undertaken and is shown in Fig. 13 (bottom). The Ni-rich precipitate was found to be slightly rich in Si and Mn, indicating the precipitate is actually Ni, Si, Mn rich G-phase.

Fig. 14(a) presents reconstructed 3D ion maps obtained via APT from HT9 irradiated to 10 dpa at 470 °C. The microstructure incorporated in this analysis includes GBs, dislocation lines and one carbide. It clearly highlights segregation of Ni and Si at the GBs and to dislocation lines. A 2.0 at. % Ni isosurface shown in Fig. 14(b) highlights Ni segregation to different microstructures: The periodic Ni segregation lines observed in the grain boundary in the top part of the reconstructed volume are accommodation edge dislocation lines characteristic of low angle grain boundaries (LAGB) [27]. In contrast, the grain boundary in the bottom part of the volume was a

high-angle grain boundary with one carbide, rich in Cr, Mo, W and V close to it. Again, no Cr-rich α′ phase and voids were observed in this condition.

3.6. HT9 irradiated to 20 dpa at 470 °C

The exact same G-phase precipitates were observed on both TEM micrographs and ChemiSTEM maps, as shown in Fig. 15. The correlation of TEM observation and ChemiSTEM characterization about G-phase precipitates could thus obtained. In addition, G-phase precipitates were observed to nucleate closely to dislocation lines, as seen on the bright field TEM micrograph of Fig. 16.

Fig. 17(a) shows the 3D ion maps of a representative APT dataset. Two Cr-rich carbides containing Mo, V and W were found in the reconstructed volume. In addition, one Ni, Si, Mn rich precipitate was present at the GB. A 7.0 at. % Ni isosurface was applied in Fig. 17(b) in order to highlight the Ni, Si, Mn rich precipitate present in the analyzed volume. According to the geometry of the isosurface, the precipitate average size was estimated to be ~35 nm. 1D analysis along the cylindrical region of interest shown in Fig. 17(b) confirmed the Ni, Si, Mn rich precipitate was present at the GB, and
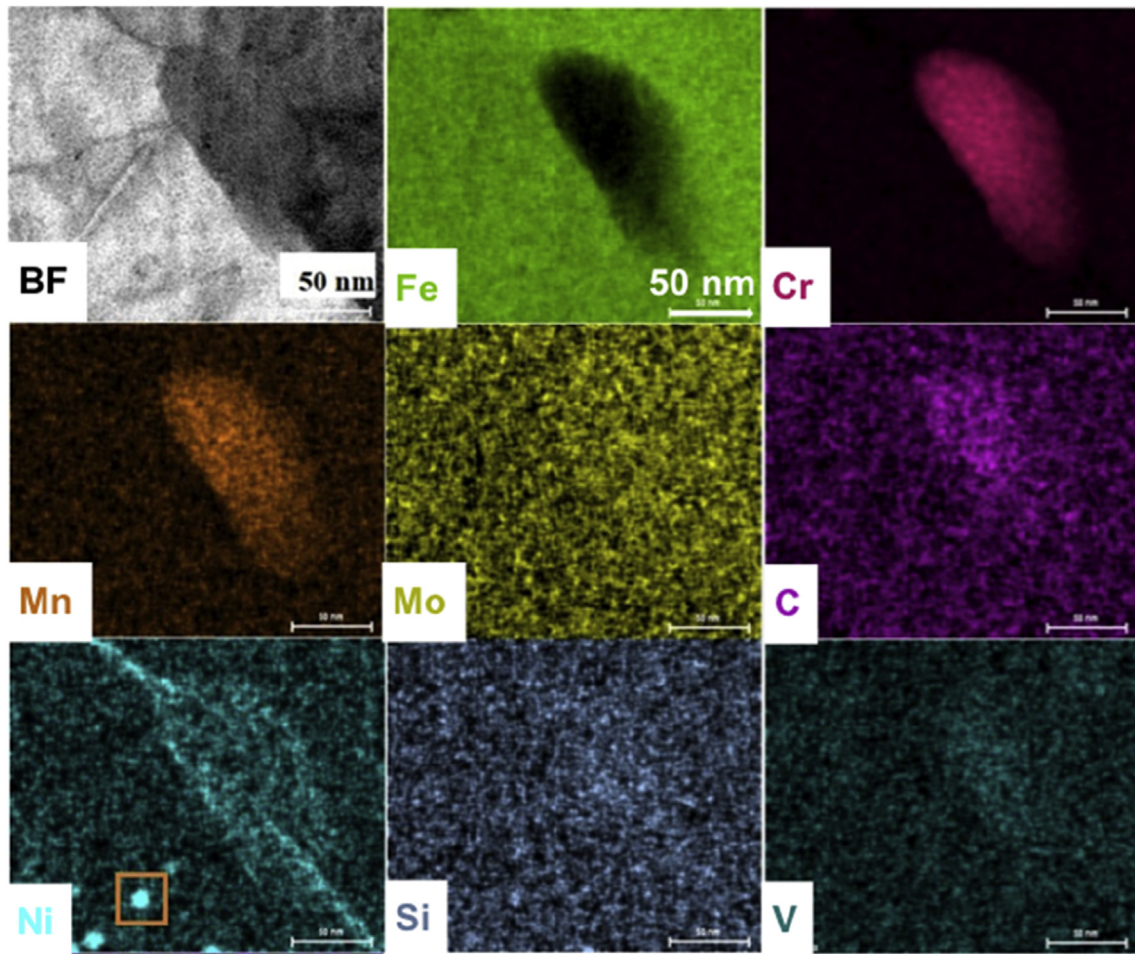
Fig. 7. Ni segregation at the GB and to the carbide/matrix interface, combined with Ni-rich precipitates (irradiation depth ~400—600 nm) were observed in HT9 irradiated to 20 dpa at 440 °C.
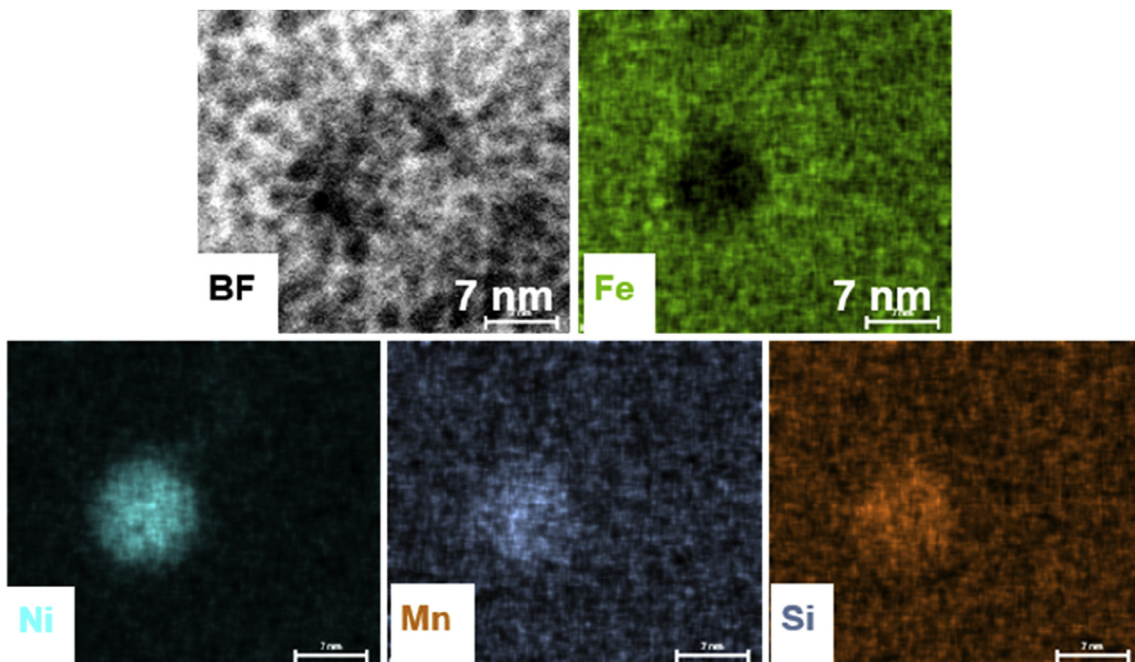
Fig. 8. ChemiSTEM maps in high magnification revealed the Ni-rich precipitate encircled in Fig. 7 is actually Ni, Si, Mn rich precipitate.
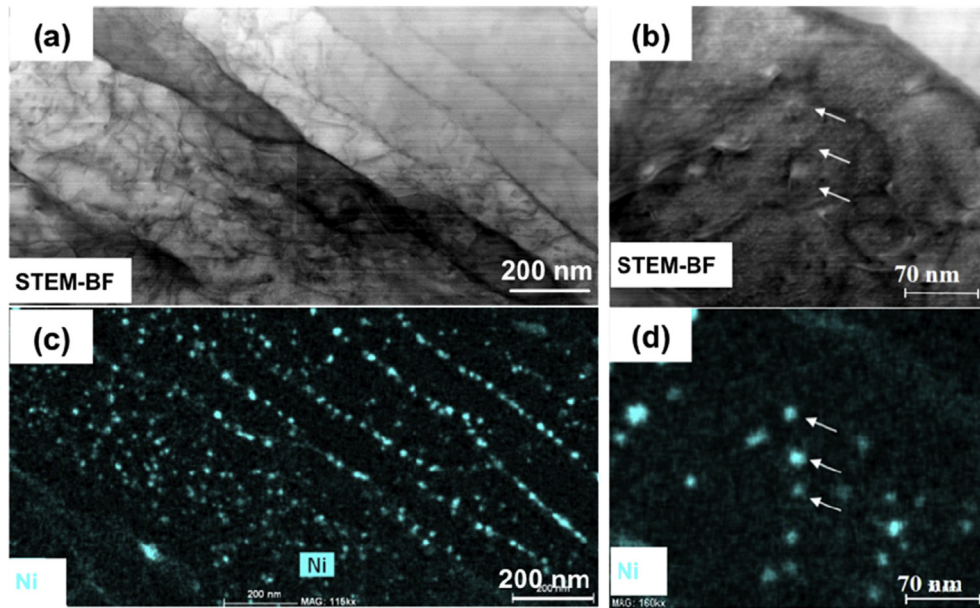
Fig. 9. STEM bright field micrographs (a-b) and corresponding Ni maps (c-d) (irradiation depth ~500–1200 nm) showed Ni, Si, Mn rich precipitates nucleated heterogeneously along lath grain boundaries and at dislocations in HT9 irradiated to 20 dpa at 440 °C.

revealed the Ni, Si segregation to the carbide/matrix interface and at the GB.

3.7. Quantitative analysis of G-phase precipitates

In the ChemiSTEM characterization, the size distribution, average size and number density of G-phase precipitates were measured on panoramas of Ni maps in HT9 irradiated to the same dose (20 dpa) at 420, 440 and 470 °C. In total, 720, 623 and 445 G-phase precipitates were identified in the conditions of 420, 440 and 470 °C, respectively. Fig. 18(a) shows the size distribution (%) histograms of G-phase precipitates identified in all three conditions. The bin width was set as 1 nm. For 420 °C, the equivalent diameter ranges from 4.49 to 29 nm centered on 11.6 nm. For 440 °C, the equivalent diameter ranges from 6.3 to 30.8 nm centered on 13.72 nm. For 470 °C, the equivalent diameter ranges from 7.45 to 30.63 nm centered on 16.54 nm. The size distribution (%) showed a significant shift towards large size region when increasing the temperature from 420 to 470 °C. As shown in Fig. 18(b), the average equivalent diameters of G-phase are 11.6 ± 2.8, 13.72 ± 3.1 nm and 16.54 ± 3.53 nm for 420, 440 and 470 °C, respectively. The standard deviation of size distribution (%) was selected as the error bar of the average size. The number density of G-phase are $(10.68 \pm 1.07) \times 10^{20}$ m^{-3}, $(9.0 \pm 0.9) \times 10^{20}$ m^{-3} and $(8.26 \pm 0.83) \times 10^{20}$ m^{-3} for 420, 440 and 470 °C, respectively. The error bar of the number density relies on the inaccuracy of thickness measurement by EELS (~10%, as described already in section 2.2).

In the APT analysis, G-phase size and density were measured in the selected analyzed volumes, as shown in Fig. 18(c). Results of the G-phase average size identified by APT are compatible with those obtained by ChemiSTEM except for the condition of 470 °C. Results of the G-phase number density by APT are less comparable with those obtained by ChemiSTEM. The discrepancy between results is probably due to the limited statistical data for the measurement done by APT due to it relatively small analysis volumes. In fact, only the G-phase precipitates localized in the studied small volume could be identified. As a result, only a small amount of G-phase

were measured by APT. Therefore, results obtained by ChemiSTEM are likely more globally representative for quantifying the radiation-induced G-phase in irradiated HT9. The average size and number density identified by both ChemiSTEM and APT showed a noticeable dependence on irradiation temperature. With the same irradiation dose, the average size of G-phase increased whereas the number density decreased with increasing irradiation temperature.

Fig. 19(a) shows the spatial distribution of G-phase precipitates in HT9 irradiated to 20 dpa at 420 °C. The SRIM simulated damage profile was inserted in Fig. 19(a). The distribution of G-phase was found to be dependent on the damage profile. As seen in Fig. 19(a), the G-phase precipitates were only observed in the irradiated area (depth < 1400 nm) at 420 °C. No G-phase precipitates were observed in the non-irradiated area (depth > 1400 nm), meaning that the temperature alone is not sufficient to induce the G-phase precipitation without irradiation. The heterogeneous distribution of G-phase was also observed in the condition of 20 dpa at 440 and 470 °C. However, figures similar to Fig. 19(a) are not shown here in order to avoid repeating the similar description.

Because FIB lift-out specimens keep a cross-section geometry of bulk samples, the evolution of G-phase average size can be thus plotted as a function of irradiation depth. The bin width was set as ~100 nm depth for plotting Fig. 19(b). The average equivalent diameter of G-phase in each bin as a function of irradiation depth was shown in Fig. 19(b). With the same irradiation temperature, the average size increased with increasing irradiation depth (dose). The average equivalent diameter increases significantly with increasing irradiation depth (dose) at 420 and 440 °C. However, it has less significant variation with increasing irradiation depth (dose) at 470 °C.

4. Discussion

4.1. Radiation induced segregation

In this study, radiation-induced Ni and Si segregation at grain boundaries and to dislocation lines was observed in all irradiation conditions. In addition, Cr depletion combined with other solutes
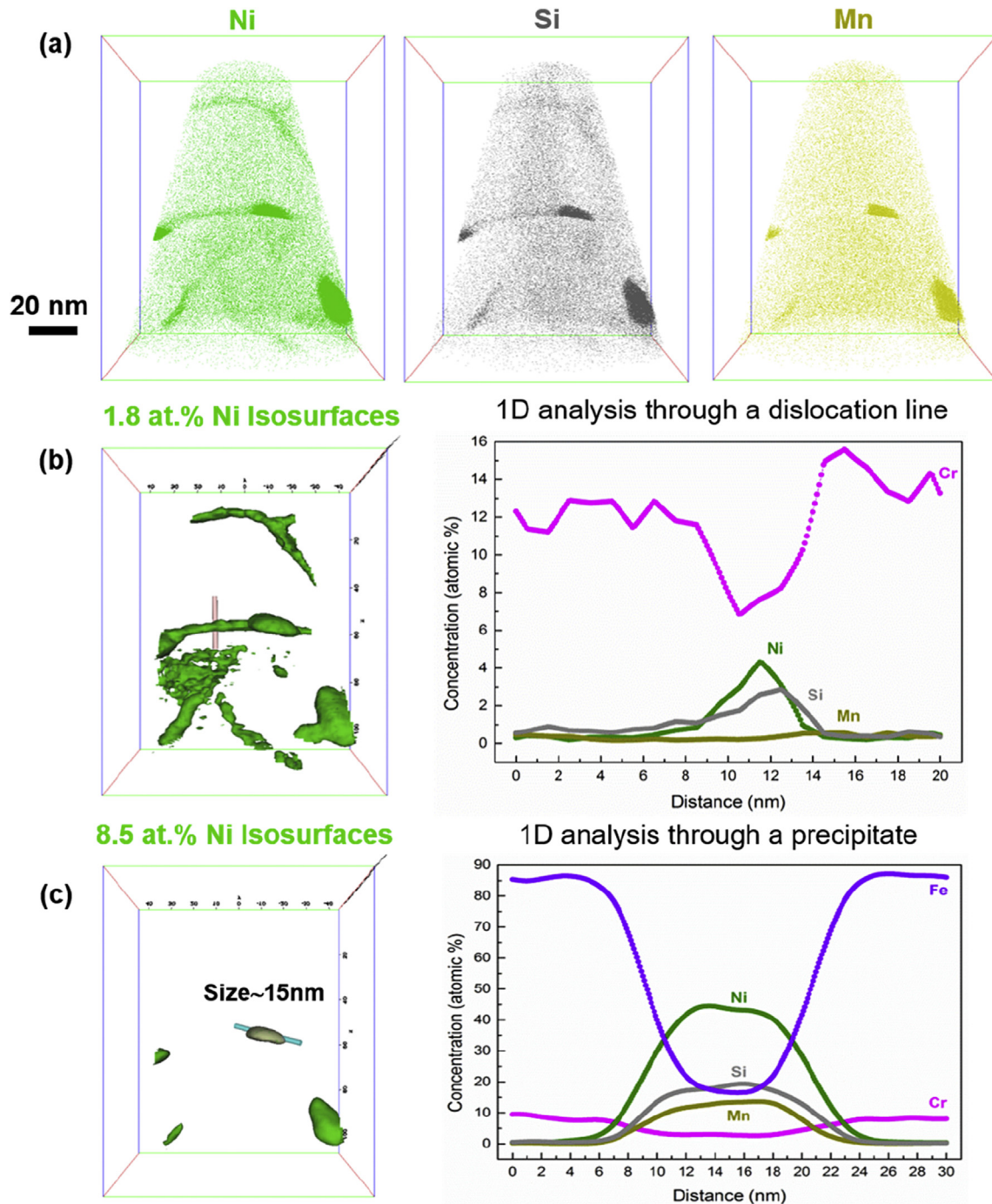
Fig. 10. (a). 3D ion maps from HT9 irradiated to 20 dpa at 440 °C. Ni and Si segregation to dislocation lines was observed together with Ni-Si-Mn precipitates. (b). 1D analysis cylinder through one of dislocation lines in HT9 irradiated to 20 dpa at 440 °C. (c). 1D Analysis cylinder through one of Ni, Si, Mn rich precipitates in HT9 irradiated to 20 dpa at 440 °C.

depletion (Mn and V) were usually observed in the grain boundaries where Ni and Si segregated. Ni and Si segregation to the carbide/matrix interface was also observed in some of irradiation conditions, highlighting the role of the interface as a sink for point defects. This is consistent with previous reports of F/M steel [28]. Jiao et al. [29] reported Ni, Si and P to the carbide/matrix interface in HT9 irradiated to 7 dpa at 400 °C under 2 MeV proton irradiation.

As for chromium solute, the literature reports conflicting behavior in both neutron and ion irradiated F/M steels i.e. both radiation induced segregation and depletion of Cr have been reported in the literature [30]. The irradiation temperature seems to

have an influence on enrichment/depletion of Cr; Clausing et al. [31] observed Cr enrichment in the 12Cr F-M alloy HT9 following fast neutron irradiation to 13dpa at 410 °C. When performing their experiment at higher temperature (520 and 565 °C), they observed very little segregation. The influence of the grain boundary type and orientation on the segregation/depletion behavior remains also a question of interest. Choudhury et al. [32] suggested that Cr is the fastest diffusing species at all temperatures both for vacancy and interstitial diffusion, and the observed RIS behavior of Cr is a balance between two opposing mechanisms. The actual balance depends on the presence and spatial distribution of sinks as well as
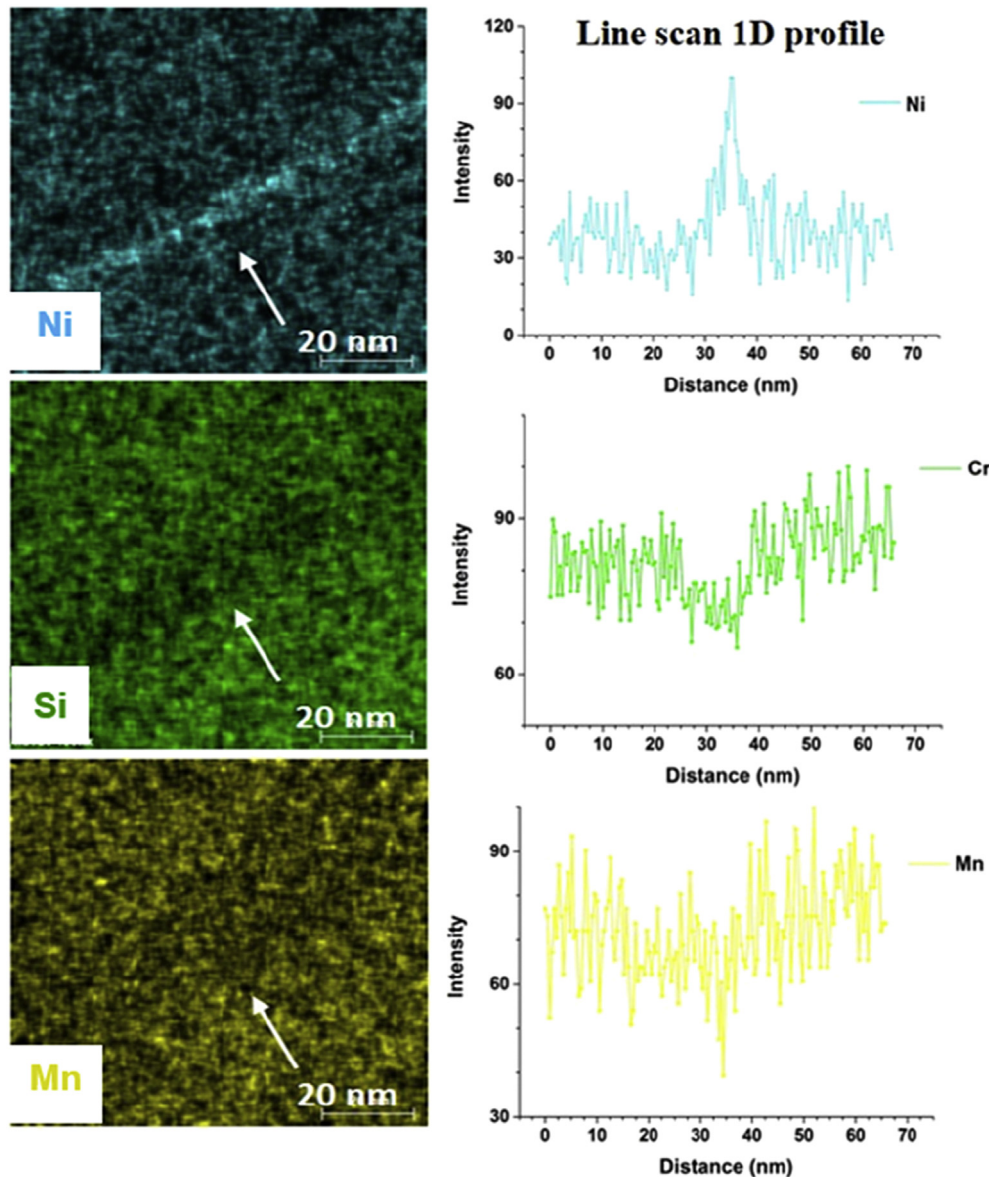
Fig. 11. ChemSTEM maps and corresponding 1D line scan profiles showed the correlation of Ni segregation with Cr and Mn depletion at the grain boundary in HT9 irradiated to 1 dpa at 470 °C.

solute concentration. Hu et al. [28] thus suggested that for the high-angle boundaries, the sink strength is much stronger therefore the vacancy mechanism works as a dominant process; however, for a coherent/low-sigma boundary, fewer sinks are present and the interstitial mechanism is the main process which gives rise to the Cr segregation.

4.2. Radiation induced precipitation

The formation of Ni, Si, Mn rich G-phase precipitates was found in HT9 irradiated to 10 dpa at 470 °C and to 20 dpa at 420, 440 and 470 °C. Among these irradiation conditions, a heterogeneous spatial distribution for G-phase was usually found. As shown in Fig. 19(a), no precipitation was observed in the non-irradiated part (irradiation depth > 1400 nm) of the specimen, indicating that temperatures alone are not sufficient to induce the G-phase precipitation without irradiation. Even with irradiation, the formation of G-phase was not observed in HT9 irradiated to 1 dpa at 470 °C,

although Ni and Si segregation was observed at such a low dose level. In contrast, G-phase precipitates were found in HT9 irradiated to 10 and 20 dpa at the same temperature (470 °C), indicating that there may exist a threshold dose for radiation induced precipitation. Similar results have been reported in T91 which is a 9Cr F/M steel of interest under proton irradiation at 400 °C [29]: A high density of G-phase precipitates was observed in T91 irradiated to 7 dpa whereas no G-phase was observed in the same alloy irradiated to 1 dpa at the same temperature, indicating that the minimum dose for radiation induced precipitation is between 1 and 7 dpa.

Some G-phase precipitates were found to nucleate heterogeneously at defect sinks (lath grain boundaries and dislocations), as evidenced by both ChemiSTEM and APT techniques (Figs. 9 and 10). The heterogeneous nucleation of G-phase has already been reported in HT9 neutron irradiated to 200 dpa at 420 °C [9]. In that study, the author described G-phase precipitates of 10 nm in diameter that were formed with laths, but larger sized G-phase were formed on Prior-Austenite Grain Boundaries (PAGB). In
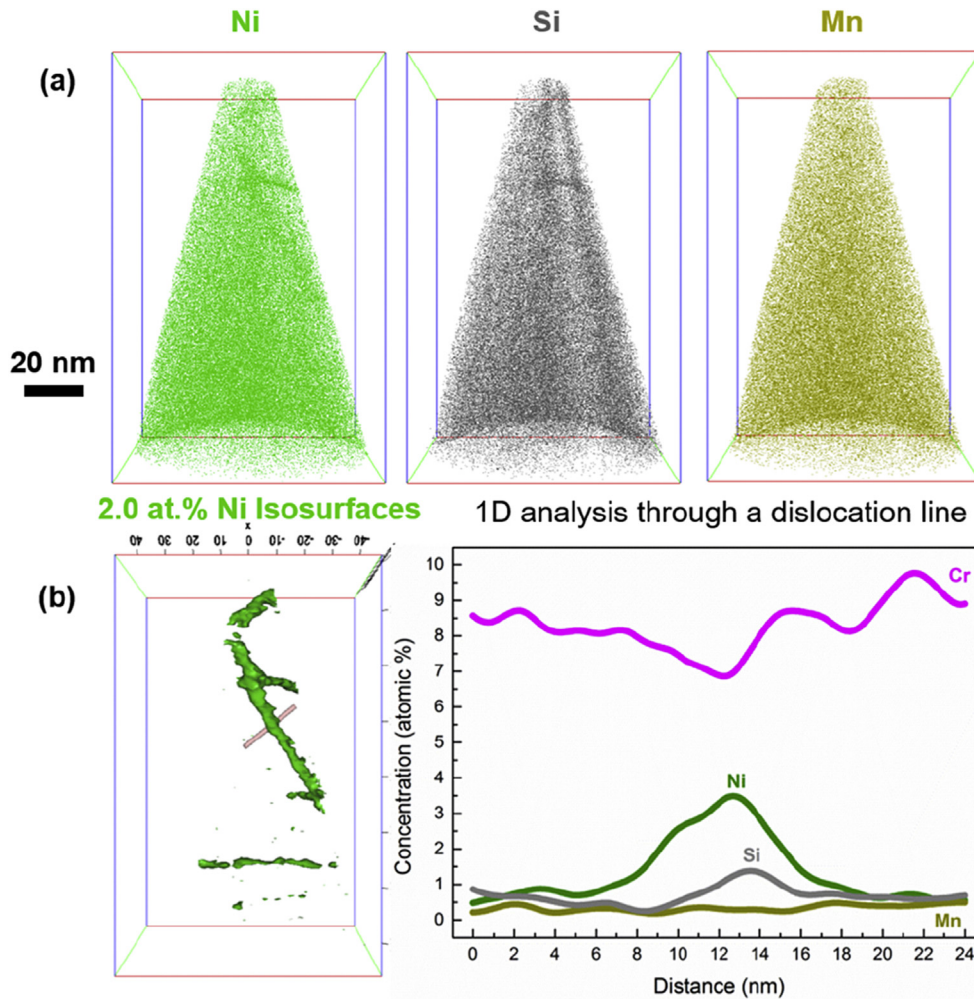
Fig. 12. (a). 3D ion maps from HT9 irradiated to 1 dpa at 470 °C. (b). 1D analysis cylinder through one of dislocation lines showed the correlation of Ni and Si segregation with Cr depletion.

addition, in the studies of Jiao et al. [29] and Wharry et al. [33], dislocations were found to be preferable nucleation sites for G-phase precipitates in F/M alloys (T91 and HT9) under ion and proton irradiations. Defect sinks are known to possess a catalytic effect on nucleation and act as favorable nucleation sites due to the possibility that nucleation process releases the excess free energy associated with defect sinks. Minor alloy elements such as Ni and Si can be considered as undersized solutes, and they are expected to segregate at defect sinks (grain boundaries, dislocations, carbide/matrix interfaces) under irradiation, leading to the nucleation of the G-phase. Again, it demonstrates radiation induced segregation plays an important role on forming radiation induced precipitation.

In neutron irradiated HT9, Anderoglu et al. [5] reported observations of a high density of Cr rich α′ precipitates together with a moderate density of G-phase precipitates with average sizes of ~ 4−11 nm respectively in 20 dpa at 380 °C. The average size of G-phase increased up to 27 nm in 155dpa at 440 °C comparing to 4−11 nm in 20 dpa at 380 °C, and the density of G-phase decreased with increasing irradiation temperature. In our study, the average size and number density of G-phase identified by both ChemiSTEM and APT showed a noticeable dependence on irradiation temperature and dose. With the same irradiation dose, the average size of G-phase increased whereas the number density decreased with increasing irradiation temperature (Fig. 18(a-b)). Within the same

irradiation temperature, the average size increased with increasing irradiation dose. Moreover, the variation of G-phase average size was less significant in the highest temperature at 470 °C comparing to 420 °C and 440 °C (Fig. 18(c)) when increasing the irradiation dose.

Cr rich α′ precipitates were not observed in any ion irradiation conditions reported in this study, whereas it has been widely observed in HT9 under neutron irradiation, indicating that α′ formation is dose dependent. Such observation was studied by Pareige et al. [34] who reported a striking difference in microstructures between ion and neutron irradiation at the some dose (0.5−0.6 dpa) and the same temperature (300C): a very high number density $(2 \times 10^{24} \text{ m}^{-3})$ of Cr rich α′ precipitates were only observed in their neutron irradiated samples, as identified by APT and not in their ion irradiated material, which had a dose rate 3 orders of magnitude higher.

### 4.3. Comparison of APT and ChemiSTEM techniques

It is recognized that the APT analysis has a better resolution to observe radiation induced segregation to carbide/matrix interfaces and dislocation lines, which is sometimes hard to confirm on ChemiSTEM maps. Moreover, the APT analysis allows us to analyze the microstructures such as defect sinks in three dimension view,
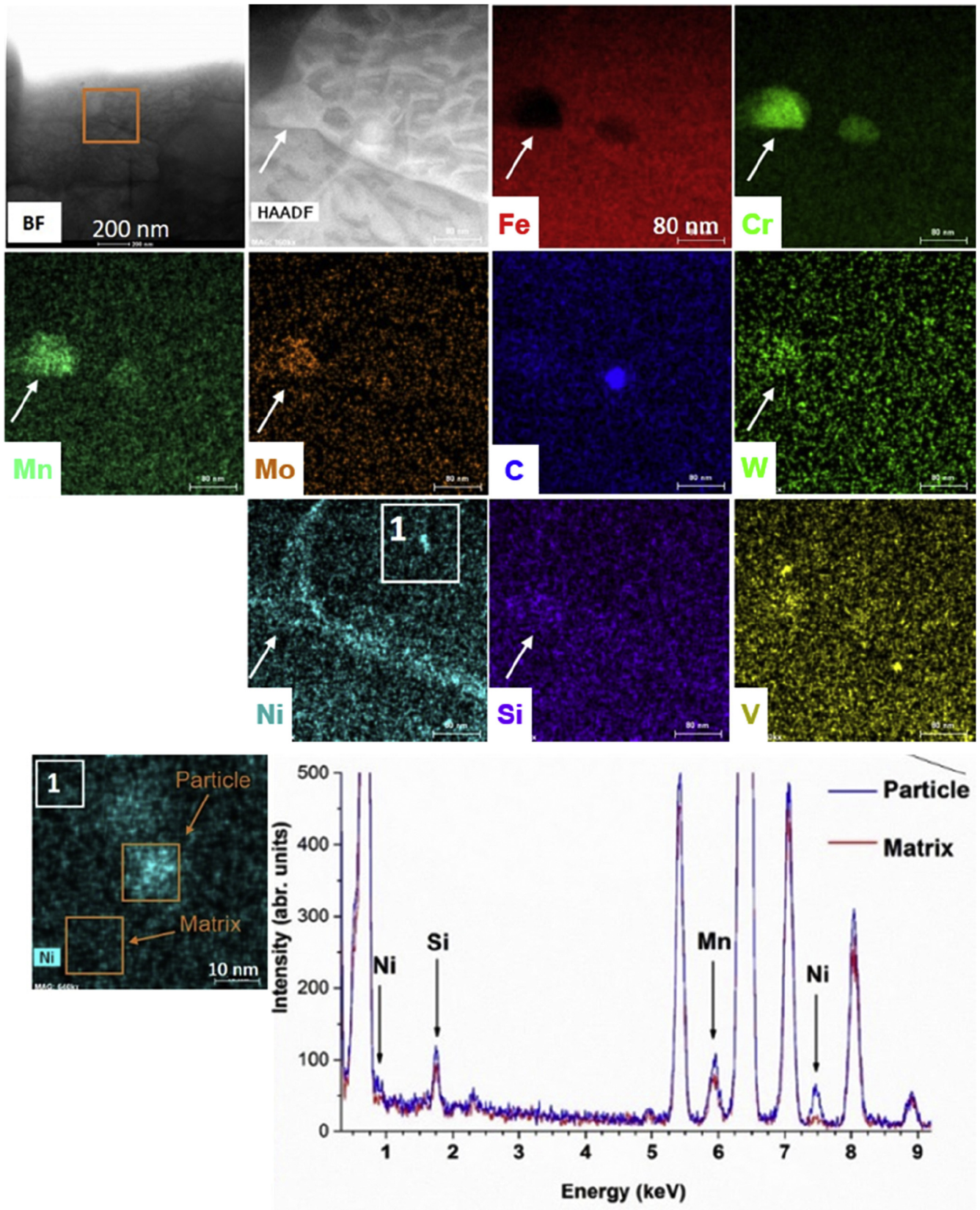
Fig. 13. (top) Ni segregation at the GB and to the carbide/matrix interface, combined with Ni-rich precipitates (irradiation depth ~200–600 nm) were found in HT9 irradiated to 10dpa at 470 °C. (bottom) The comparison of EDS spectra between the precipitate (blue) and the matrix (red) confirmed the formation of Ni, Si, Mn rich precipitates in HT9 irradiated to 10dpa at 470 °C. (For interpretation of the references to colour in this figure legend, the reader is referred to the web version of this article.)
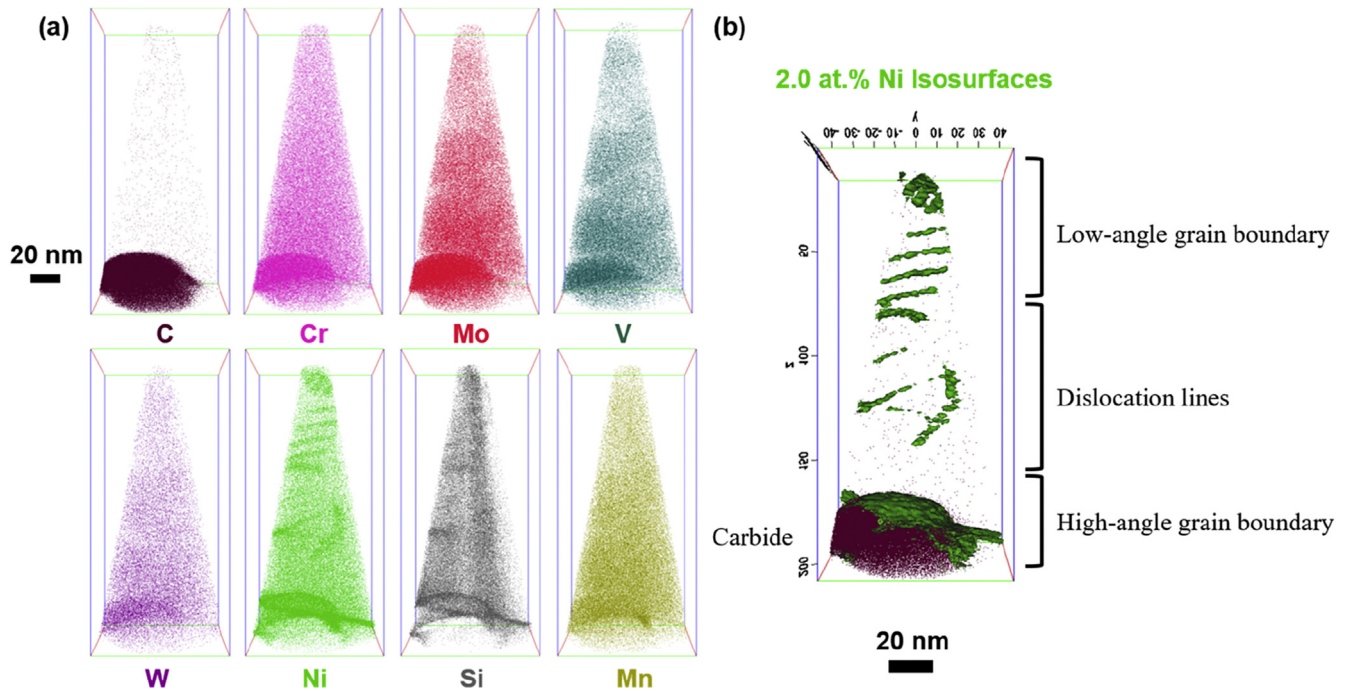
Fig. 14. (a). 3D ion maps from HT9 irradiated to 10 dpa at 470 °C. (b). 2.0 at. % Ni isosurfaces highlighting Ni segregation to the high and low angle grain boundaries and dislocation lines present in the analyzed volume.
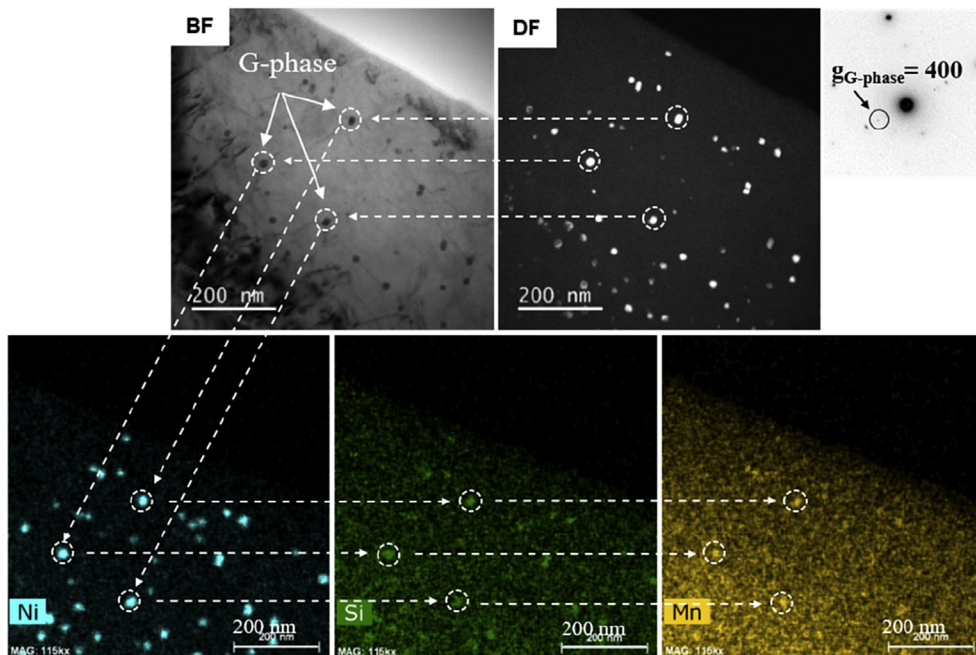
Fig. 15. Correlation of TEM observations (bright field and corresponding dark field TEM micrographs) with ChemiSTEM characterization (Ni, Si and Mn maps) for Ni, Si, Mn rich precipitates in HT9 irradiated to 20 dpa at 470 °C.

with highlighting solute enrichment. However, the information obtained by the APT is localized and is drawn from a relatively small analyzed volume. In contrast, the ChemiSTEM characterization provides more global information of microstructures such as the spatial distribution of G-phase. As a result, the size and number density of G-phase measured by the ChemiSTEM technique in this study is deemed more statistically reasonable comparing to results obtained by the APT analysis, in terms of statistic.

5. Conclusion

In this study, self-ion irradiated F/M HT9 steel to 1 and 10 dpa at 470 °C and to 20 dpa at 420, 440 and 470 °C were examined using ChemiSTEM and APT techniques. Radiation-induced Ni and Si segregation to defect sinks (grain boundaries, dislocation lines and carbide/matrix interface) was observed in all irradiation conditions. In addition, Cr depletion combined with other solutes depletion
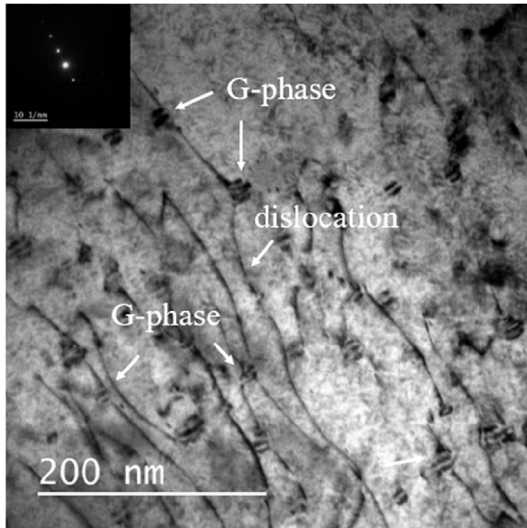
Fig. 16. Ni, Si and Mn rich G-phase precipitates nucleated heterogeneously at dislocations in HT9 irradiated to 20 dpa at 440 °C. The precipitates were represented by Moire fringes in the bright field TEM micrograph.

(Mn and V) were usually observed in the grain boundaries where Ni and Si segregated. The formation of Ni, Si, Mn rich G-phase precipitates was found in all conditions except 1 dpa at 470 °C, indicating there exists a threshold dose for radiation induced precipitation. G-phase precipitation was not observed in the non-irradiated part of specimens, indicating that temperatures alone are not sufficient to induce the G-phase precipitation without irradiation. Some of the G-phase precipitates were found to nucleate heterogeneously at defect sinks, in which Ni and/or Si segregated, suggesting defect sinks work as nucleation sites for G-phase precipitation. The average size and number density identified by both ChemiSTEM and APT showed a noticeable dependence on irradiation temperature and dose. With the same irradiation dose, the average size of G-phase increased whereas the number density decreased with increasing irradiation temperature. Within the same irradiation temperature, the average size increased with increasing irradiation dose. Apart from G-phase precipitation, no Cr-rich α' phase was found in self-ion irradiated HT9. Comparing to neutron irradiation, a significantly higher dose rate for ion irradiation is probably the main reason that no Cr-rich α' phase were formed under ion irradiation. Finally, this study serves to generate baseline data on ion irradiation effects on F/M HT9 in an effort to learn how to more accurately choose ion experimental conditions to emulate the irradiated microstructures and effects observed
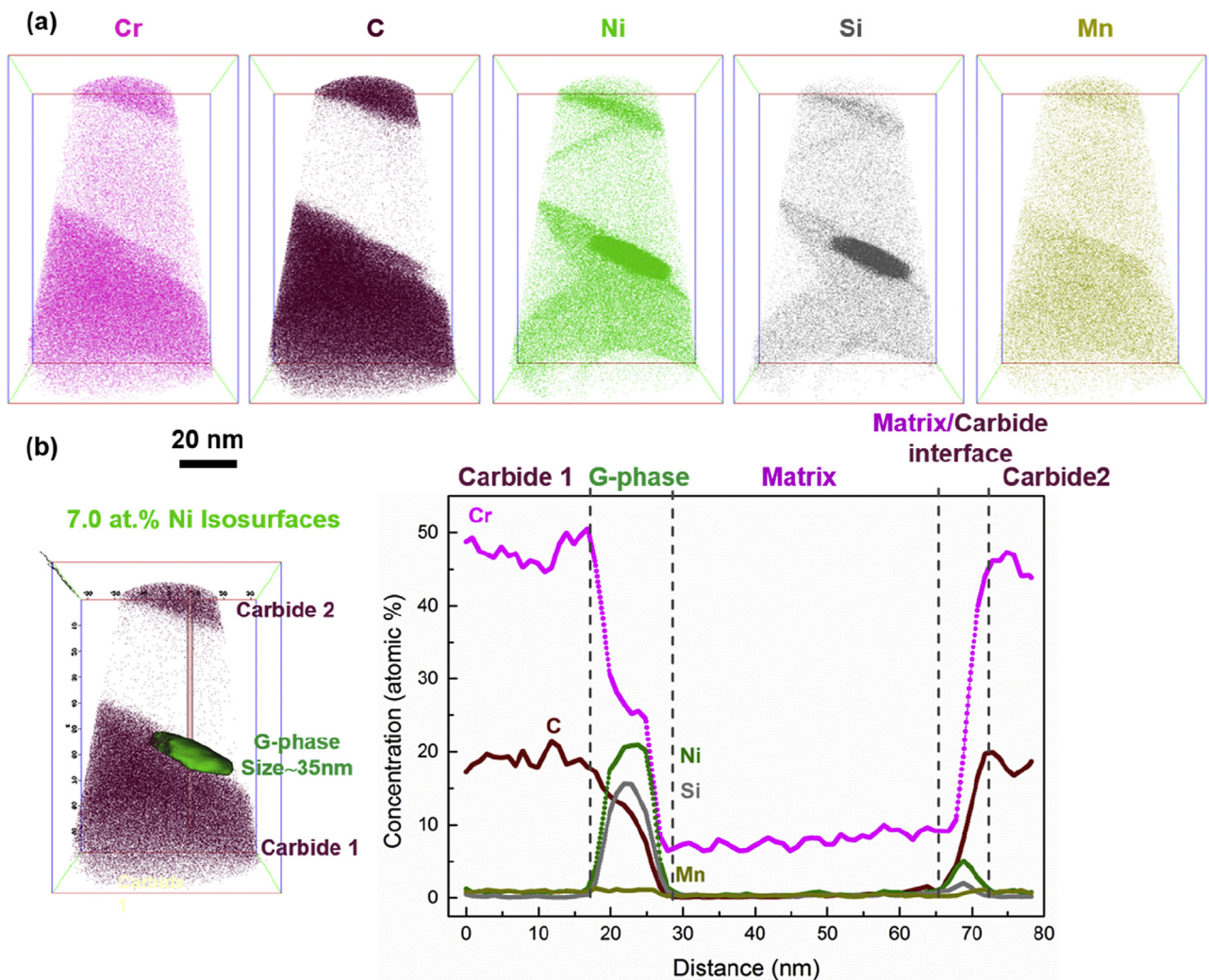
Fig. 17. (a). 3D ion maps from HT9 irradiated to 20 dpa at 470 °C. (b). 1D analysis cylinder through several interesting features in the analyzed volume: Carbides, G-phase and carbide/matrix interface.
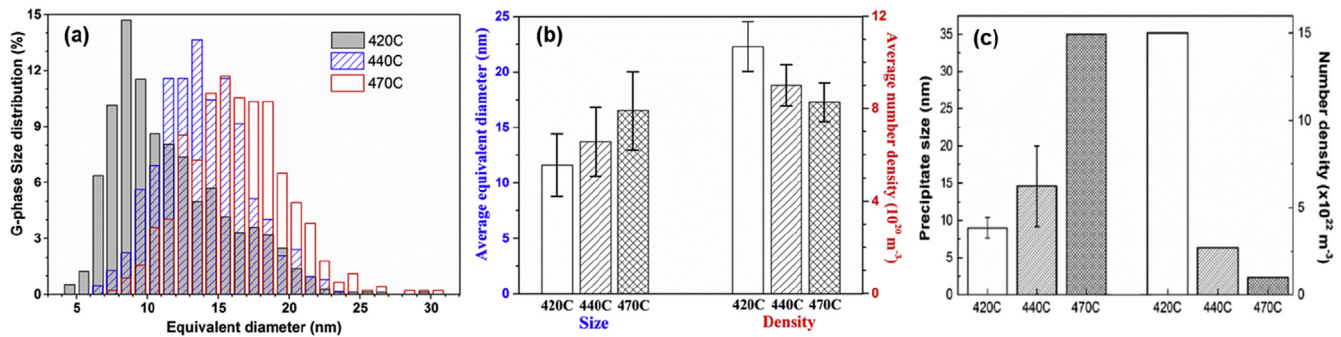
Fig. 18. (a). Size distribution (%) of G-phase precipitates as a function of their equivalent diameter in HT9 irradiated to 20 dpa at 420, 440 and 470 °C. The bin size was set as 1 nm. Quantitative analyses done by ChemiSTEM (b) and APT (c) showed the evolution of G-phase average size and number density in HT9 irradiated to the same dose (20 dpa) at different temperatures.
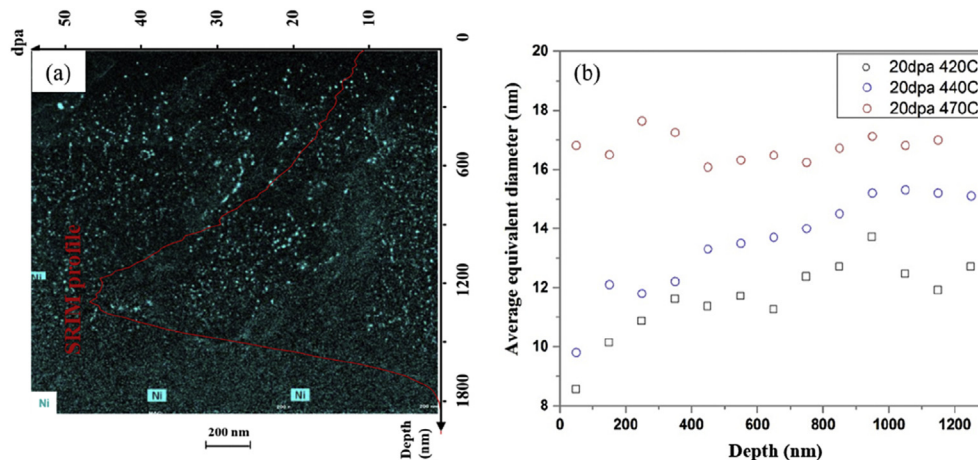
Fig. 19. (a). Ni maps with its insertion (SRIM damage profile) of HT9 irradiated to 20 dpa at 420 °C showed the heterogeneous spatial distribution of G-phase precipitates. This heterogeneous distribution was also observed in the cases of 20 dpa at 440 and 470 °C (Ni maps are not shown here). (b). Evolution of the G-phase average size in HT9 irradiated to 20 dpa at 420, 440 and 470 °C as a function of irradiation depth. The bin size was set as 100 nm depth.

under neutron irradiation.

References

[1] S.J. Zinkle, J.T. Busby, Mater. Today 12 (2009) 12.
[2] R.L. Klueh, A.T. Nelson, J. Nucl. Mater. 371 (2007) 37.
[3] F.A. Garner, R.J. Puigh, J. Nucl. Mater. 179 (1991) 577.
[4] E.A. Little, Mater. Sci. Technol. 22 (2006) 491.
[5] O. Anderoglu, J. Van den Bosch, et al., J. Nucl. Mater. 430 (2012) 194.
[6] B.H. Sencer, J.R. Kennedy, et al., J. Nucl. Mater. 393 (2009) 235.
[7] B.H. Sencer, J.R. Kennedy, et al., J. Nucl. Mater. 414 (2011) 237.
[8] J.J. Kai, R.L. Klueh, J. Nucl. Mater. 230 (1996) 116.
[9] D.S. Gelles, J. Nucl. Mater. 233–237 (1996) 293.
[10] P. Dubuisson, D. Gilbon, J.L. Seran, J. Nucl. Mater. 205 (1993) 178.
[11] P.J. Maziasz, J. Nucl. Mater. 143 (1986) 929.
[12] P.J. Maziasz, Materials for Nuclear Reactor Core Applications, vol. 2, British Nuclear Energy Society, 1988, p. 61.
[13] A. Kohyama, A. Hishinuma, et al., J. Nucl. Mater. 233 (1996) 138.
[14] E. Gaganidze, J. Aktta, Fusion Eng. Des. 88 (2013) 118.
[15] R. Chaouadi, J. Nucl. Mater. 372 (2008) 379.
[16] Y. Chen, Nucl. Eng. Technol. 45 (2013) 311.
[17] J.J. Kai, G.L. Kulcinshi, J. Nucl. Mater. 175 (1990) 227.
[18] E. Getto, K. Sun, et al., J. Nucl. Mater. 480 (2016) 159.
[19] E. Getto, G. Vancoevering, G.S. Was, J. Nucl. Mater. 484 (2017) 193.
[20] L.K. Mansur, J. Nucl. Mater. 78 (1978) 156.
[21] L.K. Mansur, Nucl. Technol. 40 (1978) 5.
[22] L.K. Mansur, J. Nucl. Mater. 206 (1993) 306.
[23] G.S. Was, Z. Jiao, et al., Scr. Mater. 88 (2014) 33.
[24] J.F. Ziegler, et al., The Stopping and Range of Ions in Solids, Pergamon, New York, 1996. See also, http://www.srim.org. for code description.
[25] N. Juslin, et al., Nucl. Instrum. Methods Phys. Res. Sect. B Beam Interact. Mater. Atoms 255 (2007) 75.
[26] T. Malis, S.C. Cheng, R.F. Egerton, J. Electron Microsc. Tech. 8 (1988) p193.
[27] V. Kuksenko, C. Pareige, C. Genevois, P. Pareige, J. Nucl. Mater. 434 (2013) 49.
[28] R. Hu, G. Smith, E.A. Marquis, Acta Mater. 61 (2013) 3490.
[29] Z. Jiao, V. Shankar, G.S. Was, J. Nucl. Mater. 419 (2011) 52.
[30] G.S. Was, J.P. Wharry, et al., J. Nucl. Mater. 411 (2011) 41.
[31] R.E. Clausing, L. Heatherly, et al., J. Nucl. Mater. 141 (1986) 978.
[32] S. Choudhury, L. Barnard, et al., J. Nucl. Mater. 411 (2011) 1.
[33] J.P. Wharry, Z. Jiao, et al., J. Nucl. Mater. 417 (2011) 140.
[34] C. Pareige, V. Kuksenko, P. Pareige, J. Nucl. Mater. 456 (2015) 471.